Supporting information

Trace Electrolyte Additive Dynamically Regulating the Zinc Anode Interface Towards Stable Zinc-Based Energy Storage

Xinyu Yang, Ke Zhang, Liubing Dong *

College of Chemistry and Materials Science, Jinan University

* Corresponding author: donglb@jnu.edu.cn

Supporting Figures and Tables

Figure S1. Flammability tests of the $ZnSO_4$/GB hybrid electrolytes-saturated glass fiber membranes. For an intuitive understanding, a corresponding image of flammable ethanol is also displayed (the right-most image). The aqueous $ZnSO_4$/GB hybrid electrolytes with various GB concentrations are nonflammable.

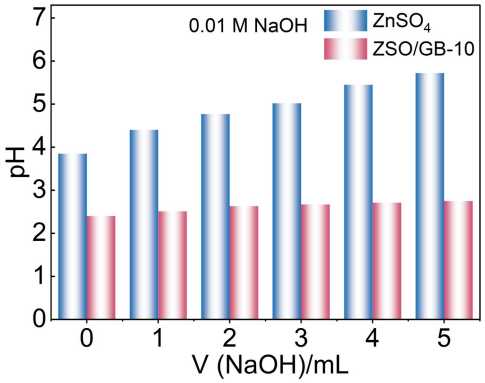

Figure S2. Titration curves of the $ZnSO_4$ and ZSO/GB-10 electrolytes. The pH of the pure $ZnSO_4$ electrolyte exhibits a significant change with the increasing amount of introduced OH^-, while the pH of the ZSO/GB-10 electrolyte remains relatively stable. This also validates that the hydrolysis of the GB additive is reversible and the electrolyte pH is dynamically regulated.

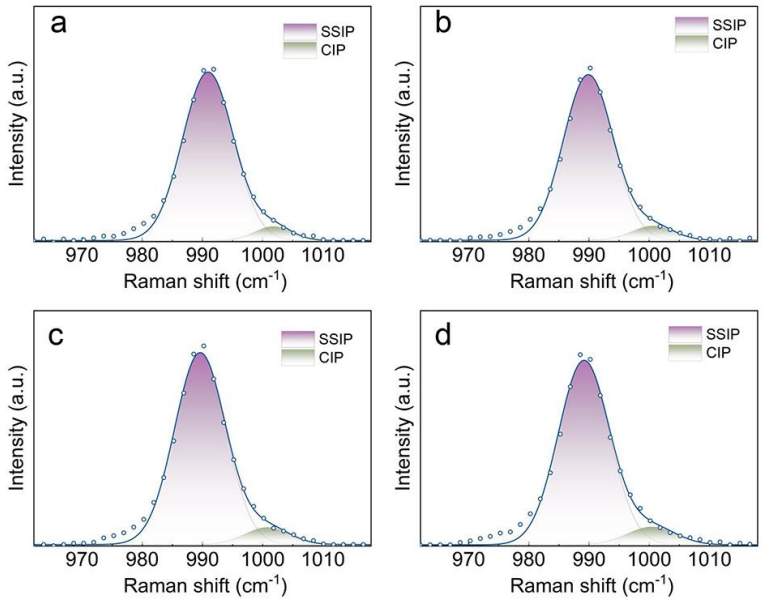

Figure S3. Raman spectra of SO_4^{2-} signals in (a) the ZSO/GB-5, (b) ZSO/GB-15, (c) ZSO/GB-25 and (d) ZSO/GB-50 electrolytes.

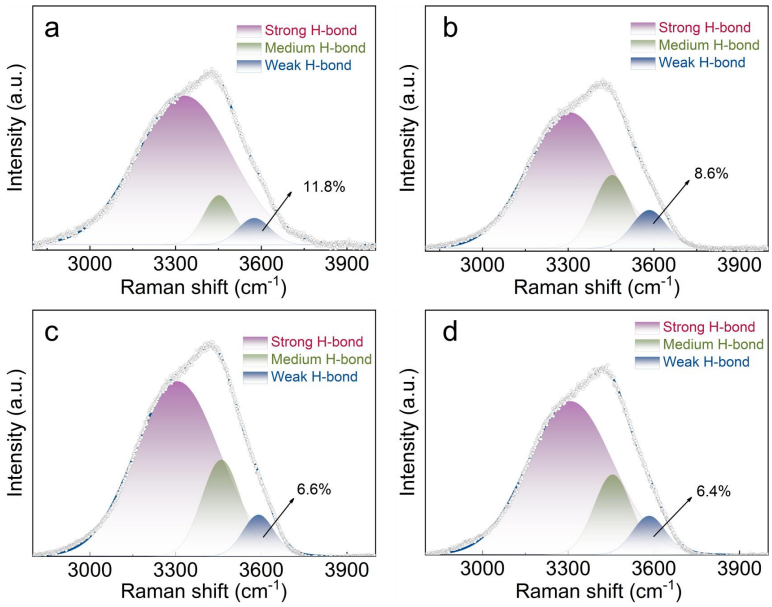

Figure S4. Raman spectra of H-bond signals in (a) the ZSO/GB-5, (b) ZSO/GB-15, (c) ZSO/GB-25 and (d) ZSO/GB-50 electrolytes. As the GB content increases, the proportion of the weak H-bond first rises and then decreases. The initial increase occurs because the GB replaces active water molecules in the Zn^{2+} solvation shell, disrupting the H-bond network and suppressing HER at the zinc anode interface caused by active water. As the GB content increases, the electrolyte pH decreases. The reduced pH leads to higher H^+ concentration in the electrolyte, strengthening H-bond and reducing weak H-bond.

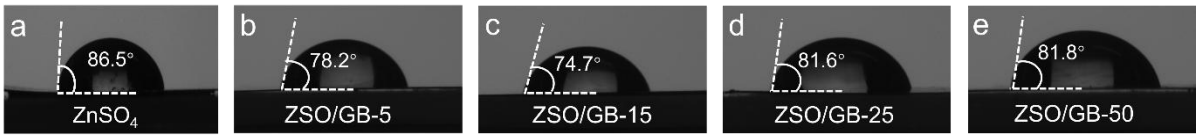

Figure S5. Contact angles of (a) the $ZnSO_4$, (b) the ZSO/GB-5, (c) ZSO/GB-15, (d) ZSO/GB-25 and (e) ZSO/GB-50 electrolytes. Compared to the $ZnSO_4$ electrolyte, $ZnSO_4$/GB hybrid electrolytes exhibit smaller contact angles on the zinc foil, demonstrating a favorable zinc affinity. Note that the $ZnSO_4$/GB hybrid electrolytes with high GB concentrations, such as 50 mM, show relatively large contact angles. This is because the $ZnSO_4$/GB hybrid electrolytes with high GB concentrations possess relatively high viscosity to reduce their fluidity, thereby showing an increased contact angle on zinc anodes.

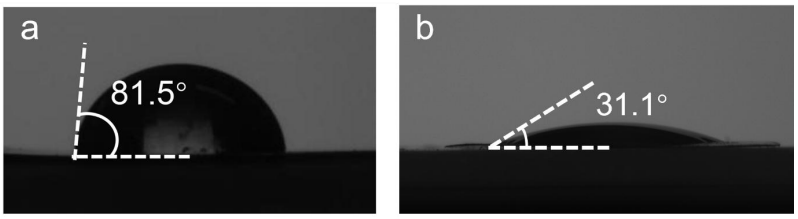

Figure S6. Water contact angles of (a) the bare zinc foil and (b) the zinc foil after soaking in the GB aqueous solution for 24 h.

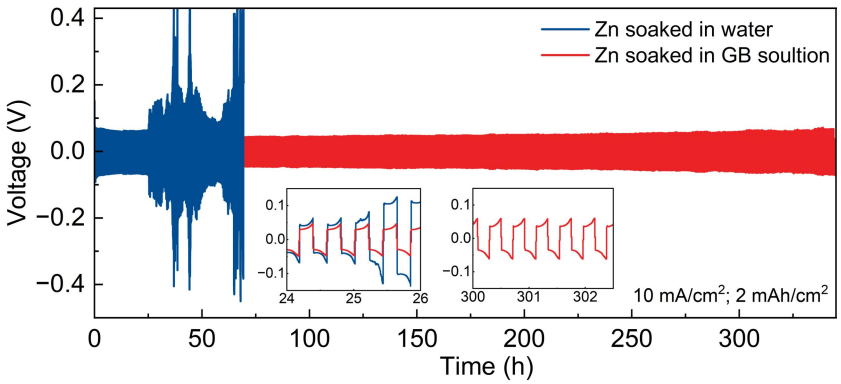

Figure S7. Cycling performance of Zn//Zn symmetric cells assembled with the zinc foil electrode after soaking in the deionized water or 10 mM GB aqueous solution for 24 h (testing condition: 10 mA/cm^2 and 2 mAh/cm^2). 2 M $ZnSO_4$ electrolyte is utilized in the symmetric cells. After soaking in the GB aqueous solution, the zinc anode presents remarkably extended operation lifetime even in the pure $ZnSO_4$ electrolyte, which is also evidence that the hydrolyzed GB molecules spontaneously adsorb on the zinc foil and thereby positively regulate the zinc anode interface.

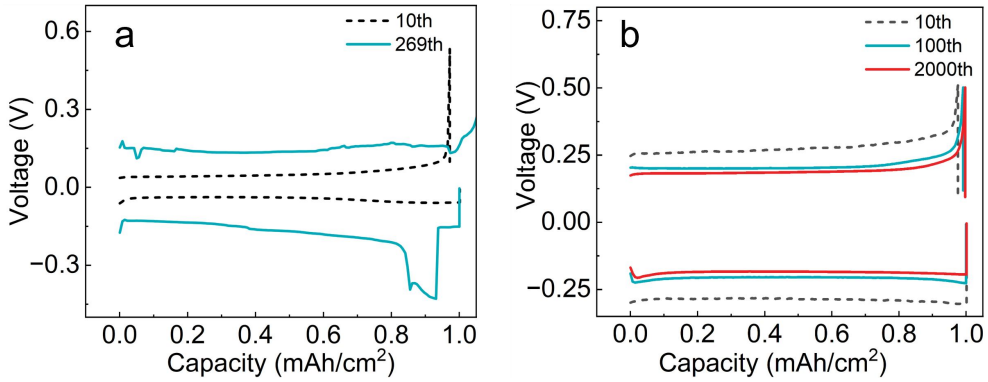

Figure S8. Voltage-capacity curves of Cu//Zn asymmetric cells using (a) the $ZnSO_4$ and (b) ZSO/GB-10 electrolytes.

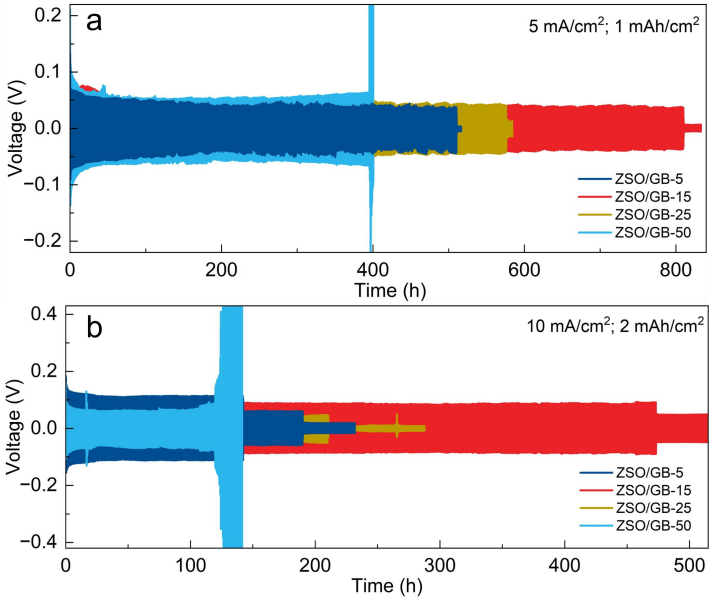

Figure S9. Cycling performance of Zn//Zn symmetric cells assembled using the $ZnSO_4$/GB hybrid electrolytes under the testing conditions of: (a) 5 mA/cm^2 and 1 mAh/cm^2; (b) 10 mA/cm^2 and 2 mAh/cm^2.

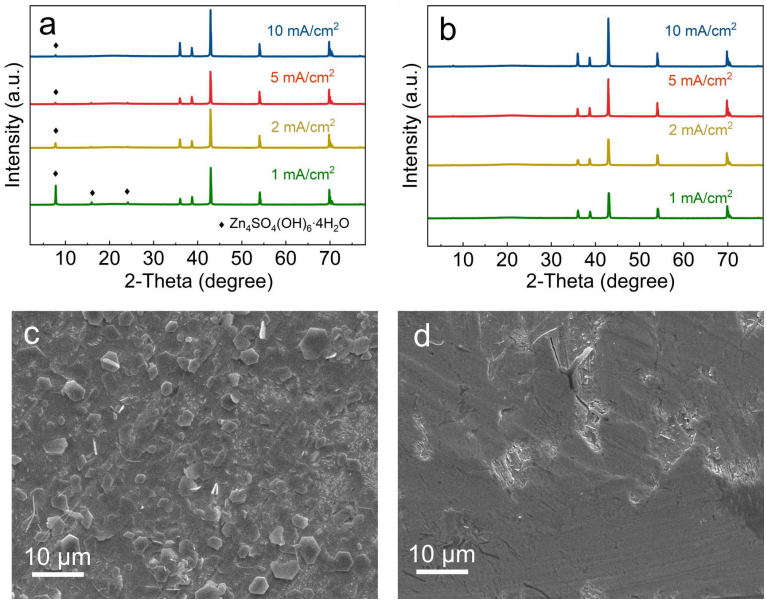

Figure S10. XRD patterns of the zinc anodes after 50 charge/discharge cycles at different current densities in (a) the $ZnSO_4$ and (b) ZSO/GB-10 electrolytes. SEM images of the zinc anodes after 50 cycles at a current density of 5 mA/cm^2 in (c) the $ZnSO_4$ and (d) ZSO/GB-10 electrolytes. The zinc anodes after cycling in the $ZnSO_4$ electrolyte exhibit characteristic diffraction peaks of $Zn_4SO_4(OH)_6{\cdot}4H_2O$ by-product in (a), which is associated with the occurrence of parasitic reactions at the zinc anode interface. Meanwhile, dendrite-like morphology is observed for the zinc anodes after cycling in the $ZnSO_4$ electrolyte in (c). In contrast, the ZSO/GB-10 electrolyte suppresses the generation of the parasitic reactions-induced by-product and zinc dendrites.

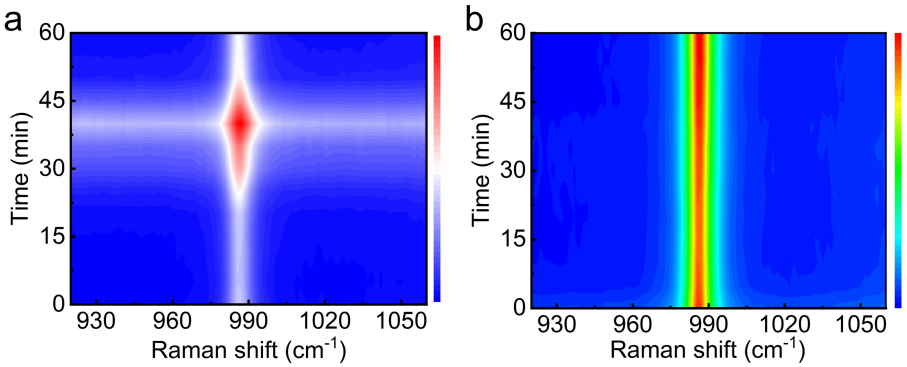

Figure S11. *In-situ* Raman spectra of SO_4^{2-} signal at the zinc anode interface in (a) the $ZnSO_4$ and (b) $ZnSO_4$/GB-10 electrolytes. A Zn//Zn symmetric cell is assembled in a cuvette, and Raman spectra at the zinc anode interface are recorded in real time during continuous charging of the cell. The *in-situ* Raman spectra in the $ZnSO_4$ electrolyte exhibit pronounced fluctuations throughout the zinc deposition process, which is ascribed to the parasitic reactions at the zinc anode interface that result in increased electrolyte pH and the consumption of SO_4^{2-} anions to generate basic zinc sulfate by-products. Differently, the SO_4^{2-} signal intensity at the ZSO/GB-10 electrolyte/anode interface remains almost unchanged, suggesting stable electrolyte pH enabled by the hydrolysis equilibrium of the GB additive, and such a stable chemistry environment of the zinc anode interface is helpful in realizing uniform zinc deposition.

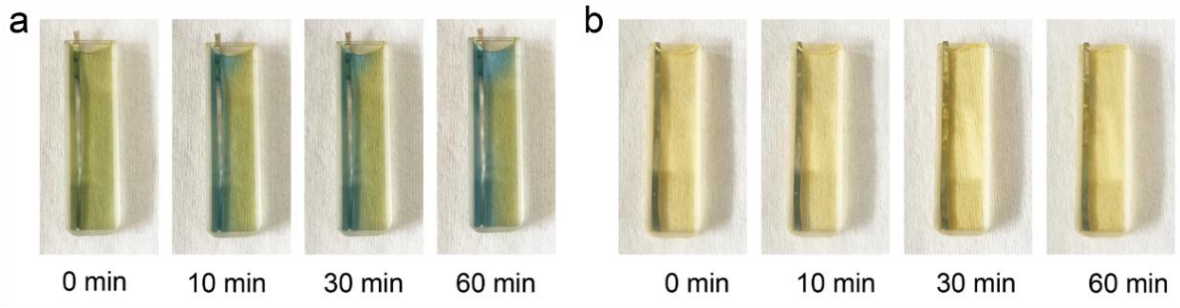

Figure S12. Photographs documenting the color change of the zinc foil immersed in the (a) $ZnSO_4$ and (b) ZSO/GB-10 electrolytes. Bromocresol green was used as a pH indicator and added to both $ZnSO_4$ and ZSO/GB-10 electrolytes, as its aqueous solution changes from yellow to blue when the pH value increases from approximately 4 to 5. The significant color change indicates a pH value increase in the $ZnSO_4$ electrolyte, resulting from the spontaneous corrosion of metallic zinc by the weakly acidic $ZnSO_4$ electrolyte. In contrast, for the ZSO/GB-10 electrolyte, although its pH is even lower than that of the 2 M $ZnSO_4$ electrolyte, there are no noticeable changes that occur around the zinc foil even though the foil is soaked in the ZSO/GB-10 electrolyte for 60 min, verifying that the hydrolyzed GB molecules adsorb on the zinc anode to inhibit zinc corrosion.

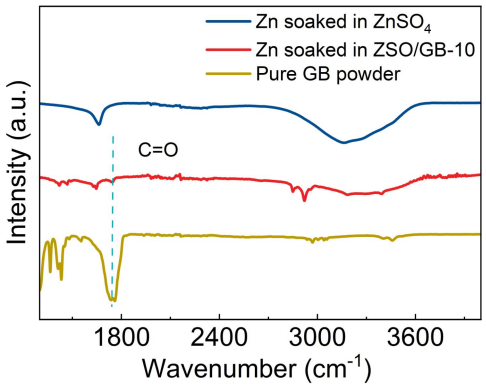

Figure S13. FTIR spectra of the zinc foil after soaking in the $ZnSO_4$ and ZSO/GB-10 electrolytes. The FTIR spectrum of the zinc foil immersed in the ZSO/GB-10 electrolyte exhibits a C=O peak at 1760 cm^{-1}, suggesting that the hydrolyzed GB molecules adsorb on the zinc anode *via* their -COOH groups, which is consistent with the analysis in Figure 2.

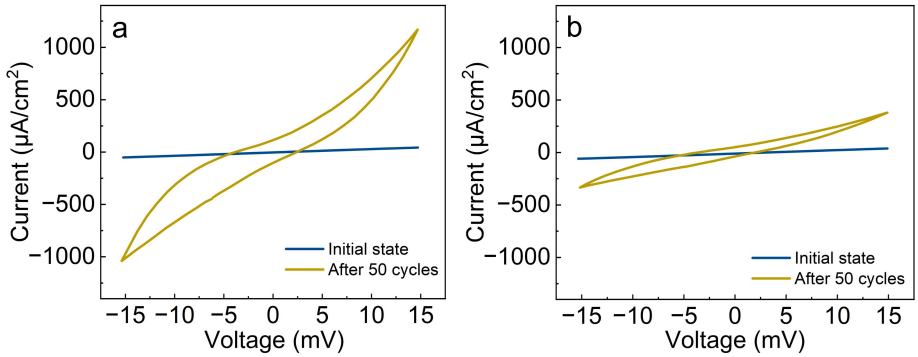

Figure S14. CV curves at a scan rate of 10 mV/s of the Zn//Zn symmetric cells using (a) the $ZnSO_4$ and (b) ZSO/GB-10 electrolytes. The symmetric cells were charged/discharged for 50 cycles under the condition of 10 mA/cm^2 and 2 mAh/cm^2.

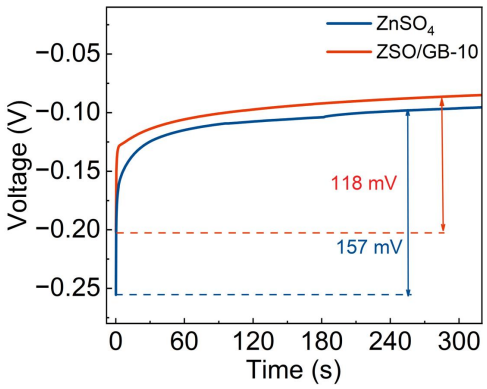

Figure S15. Zinc nucleation overpotentials at 10 mA/cm^2 in different electrolytes.

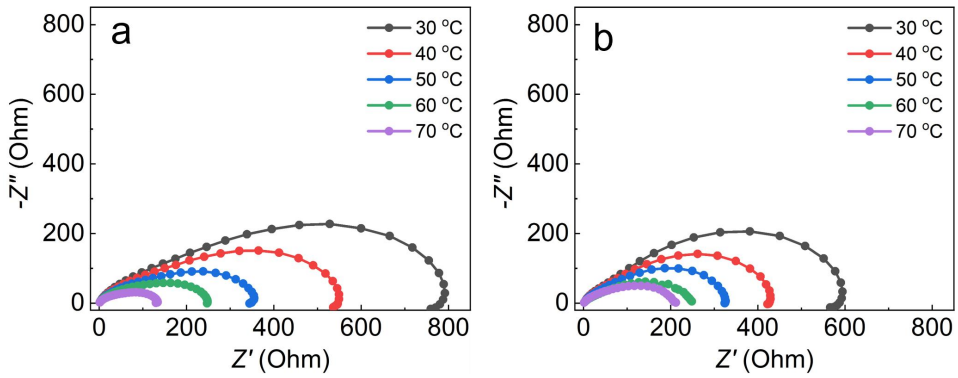

Figure S16. EIS spectra at different temperatures of the Zn//Zn symmetric cells with (a) the $ZnSO_4$ and (b) ZSO/GB-10 electrolytes.

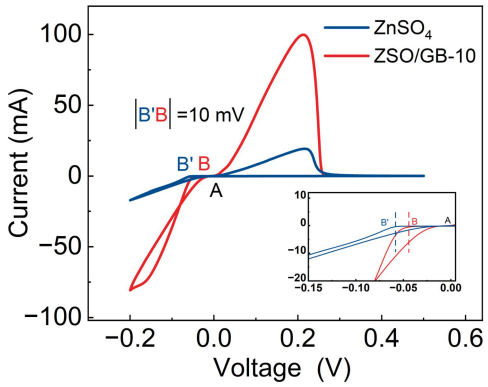

Figure S17. CV curves at 1 mV/s of the Ti//Zn asymmetric cells with different electrolytes. The |AB'| and |AB| represent the zinc nucleation overpotential in the $ZnSO_4$ and ZSO/GB-10 electrolytes, respectively. It reveals that the cell with the ZSO/GB-10 electrolyte exhibits a lower zinc nucleation overpotential and higher response current compared to the cell using the $ZnSO_4$ electrolyte.

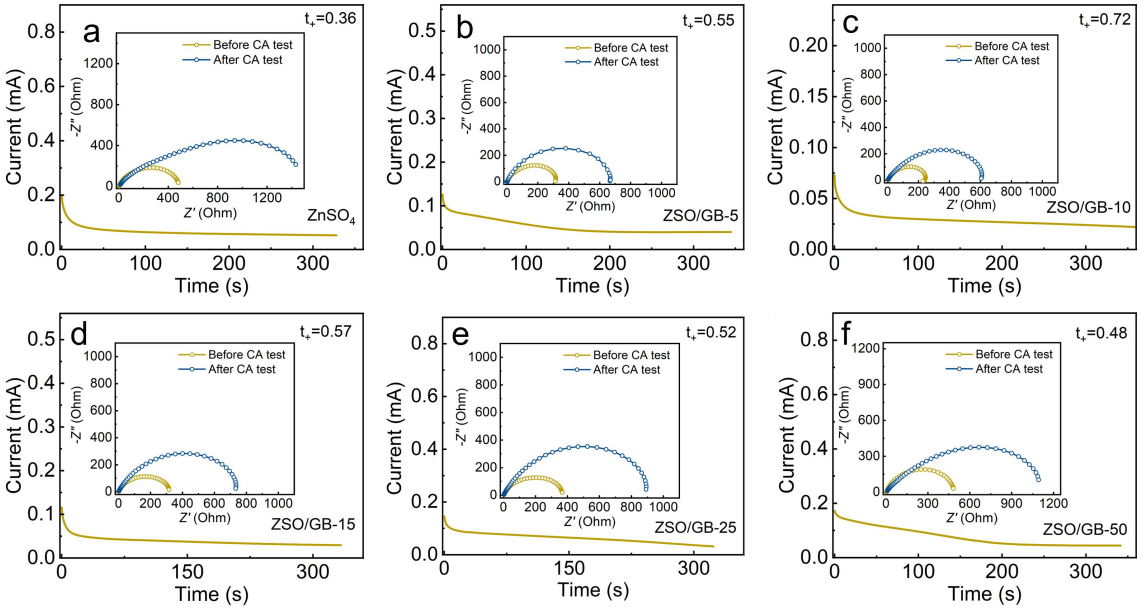

Figure S18. Zn^{2+} transference number tests for Zn//Zn symmetric cells using the electrolytes with different GB concentrations.

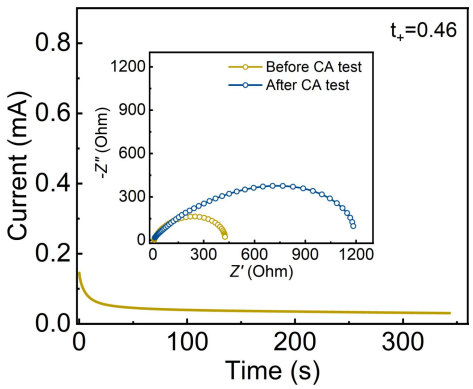

Figure S19. Zn^{2+} transference number test of Zn//Zn symmetric cells with $ZnSO_4$ electrolyte. The used zinc anodes were prepared by soaking zinc foils in 10 mM GB aqueous solution for 24 h. Such zinc anode-based Zn//Zn symmetric cells with the 2 M $ZnSO_4$ electrolyte show a Zn^{2+} transference number of 0.46, slightly larger than the Zn^{2+} transference number (0.36) of bare Zn anode-based Zn//Zn symmetric cells with the 2 M $ZnSO_4$ electrolyte, while notably lower than the Zn^{2+} transference number (0.72) of bare Zn anode-based Zn//Zn symmetric cells with the ZSO/GB-10 electrolyte. This suggests that the interfacial adsorption layer of the hydrolyzed GB molecules does exert a positive effect on Zn^{2+} transfer number, but the bulk electrolyte property is a more dominant factor affecting the Zn^{2+} transfer number in this system.

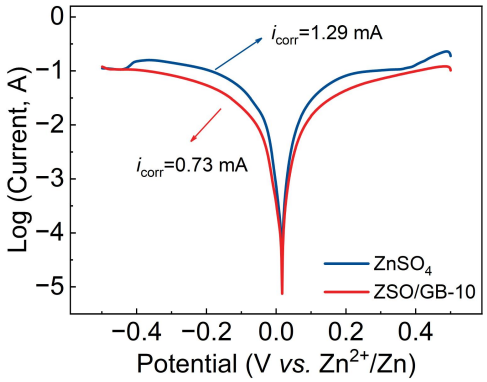

Figure S20. Tafel plots of the Zn//Zn symmetric cells with the $ZnSO_4$ and ZSO/GB-10 electrolytes. The zinc anode in the ZSO/GB-10 electrolyte presents a smaller corrosion current, indicating better anti-corrosion ability.

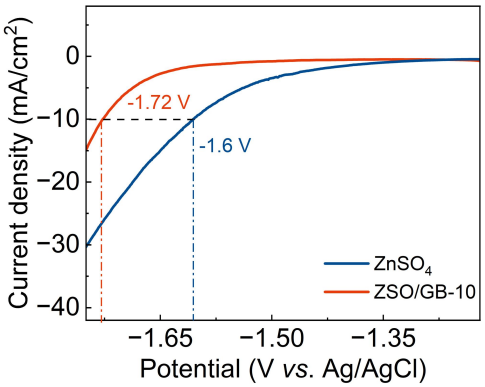

Figure S21. The LSV curves of the $ZnSO_4$ and ZSO/GB-10 electrolytes. Compared to the $ZnSO_4$ electrolyte (-1.60 V *vs.* Ag/AgCl), the ZSO/GB-10 exhibits a more negative onset potential for the HER (-1.72 V *vs.* Ag/AgCl).

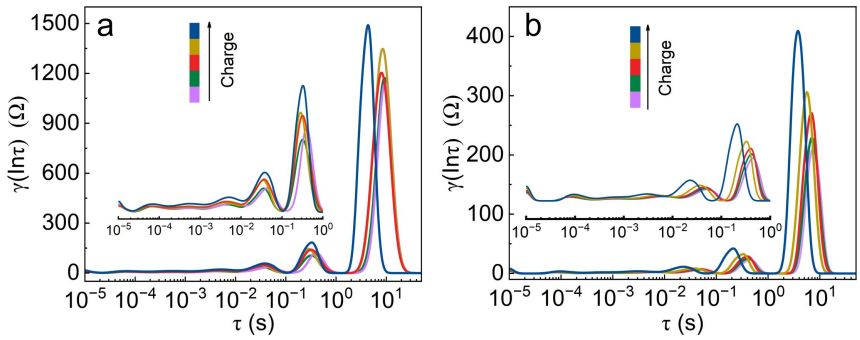

Figure S22. EIS spectra of the Zn//Zn symmetric cells with (a) the $ZnSO_4$ and (b) ZSO/GB-10 electrolytes. The charge transfer impedance (R_{ct}, which is represented by the peak in the range of $\tau=10^{-3}$-10^{-1} s) of the zinc anode in the $ZnSO_4$ electrolyte exhibits notably increasing intensity as the zinc deposition progresses, suggesting an unstable zinc anode/electrolyte interface. In contrast, the charge transfer impedance of the zinc anode in the ZSO/GB-10 electrolyte exhibits minimal variation during the zinc deposition process, indicating a relatively stable zinc anode/electrolyte interface.

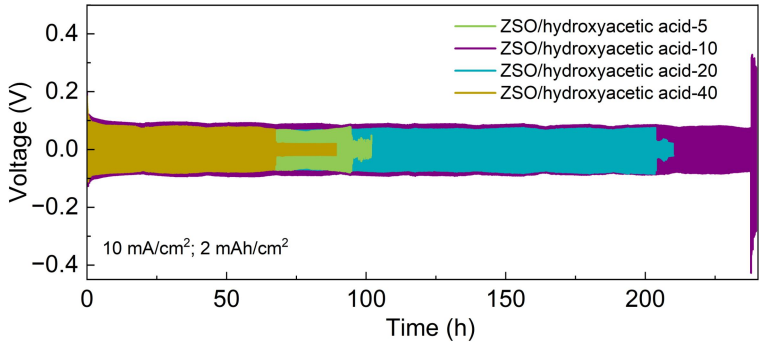

Figure S23. Electrochemical stability of Zn//Zn symmetric cells using $ZnSO_4$-based electrolytes with various concentrations of the hydroxyacetic acid additive. To identify the active species and validate the proposed dynamic regulation mechanism for the $ZnSO_4$/GB hybrid electrolytes, we prepared 2 M $ZnSO_4$/hydroxyacetic acid mixed electrolytes with hydroxyacetic acid additive concentrations set at 5, 10, 20, and 40 mM (the electrolytes were denoted as ZSO/hydroxyacetic acid-*x*, where *x* means the concentration of the hydroxyacetic acid additive). Compared with the pure $ZnSO_4$ electrolyte, adding hydroxyacetic acid to the $ZnSO_4$-based electrolyte moderately improves the cycling stability of the zinc anode, confirming the positive role of the hydroxyacetic acid component derived from the hydrolyzed GB in optimizing the zinc anode interface. Nevertheless, the cycling stability of the zinc anode in the $ZnSO_4$/hydroxyacetic acid electrolyte falls short of that observed in the ZSO/GB-10 electrolyte, suggesting that the GB additive optimizes the zinc anode interface through various ways including but not limited to the hydroxyacetic acid component.

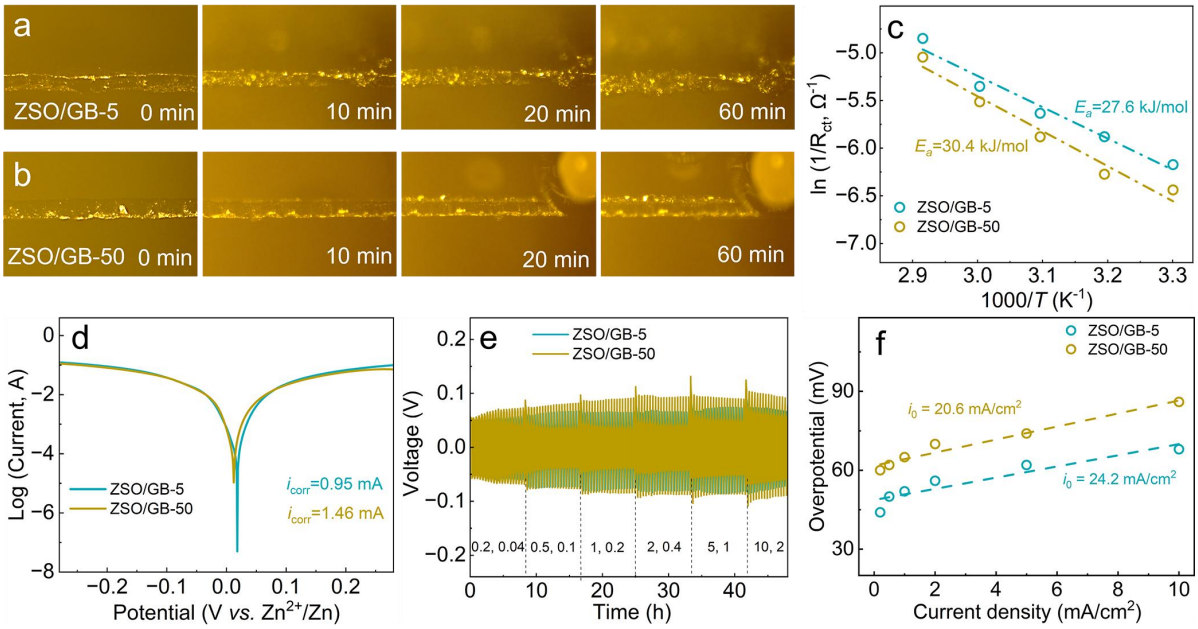

Figure S24. *In-situ* optical images of the zinc deposition morphologies in (a) the ZSO/GB-5 and (b) ZSO/GB-50 electrolytes. Zinc deposition behaviors in Zn//Zn symmetric cells with the ZSO/GB-5 and ZSO/GB-50 electrolytes: (c) Activation energy; (d) Tafel curves; (e) Rate performance and (f) corresponding exchange current density at the zinc anode interface. When the GB concentration is lower than 10 mM, the GB additive presents positive effects on the disruption of the continuous H-bond network of the electrolyte, the reduction of activation energy for Zn^{2+} desolvation process and the inhibition of anode corrosion, and the positive effects are more obvious with higher GB concentration. For instance, when the GB concentration is 5 mM, the activation energy for Zn^{2+} desolvation process is 27.6 kJ/mol, respectively. In such a case, for the very low GB concentrations such as 5 mM, there are not enough GB molecules to sufficiently regulate the electrolyte solvation structure as well as affect the zinc anode interface, thereby resulting in unsatisfactory electrochemical performance for the corresponding zinc anodes (composed with the zinc anodes in the electrolyte with the optimal GB concentration of 10 mM). On the other hand, as the GB concentration further increases, the positive effects of the GB additive are weakened due to the following reasons. From Figure 1a, we can see that the relatively high GB concentrations such as 50 mM lead to a more acidic electrolyte (*i.e.*, low pH), significantly accelerating the hydrogen evolution and anode corrosion rates, as confirmed by the large corrosion current in Figure S24d and the notably hydrogen evolution during the zinc deposition in Figure S24b. Meanwhile, the electrolyte viscosity notably increases at high GB concentrations, which is ascribed to that the hydrolyzed GB molecules strengthen intermolecular H-bond (as verified by the decreased weak H-bond proportion at high GB concentrations in Figure S2). This

raises ion transport resistance to easily induce large concentration polarization at the zinc anode interface. For instance, zinc plating/stripping process presents the largest overpotentials and the smallest exchange current density when the GB concentration is 50 mM (Figure S24f). As a result, the zinc anodes in the ZSO/GB-50 electrolyte present even inferior electrochemical performance than those in the ZSO/GB-10 electrolyte.

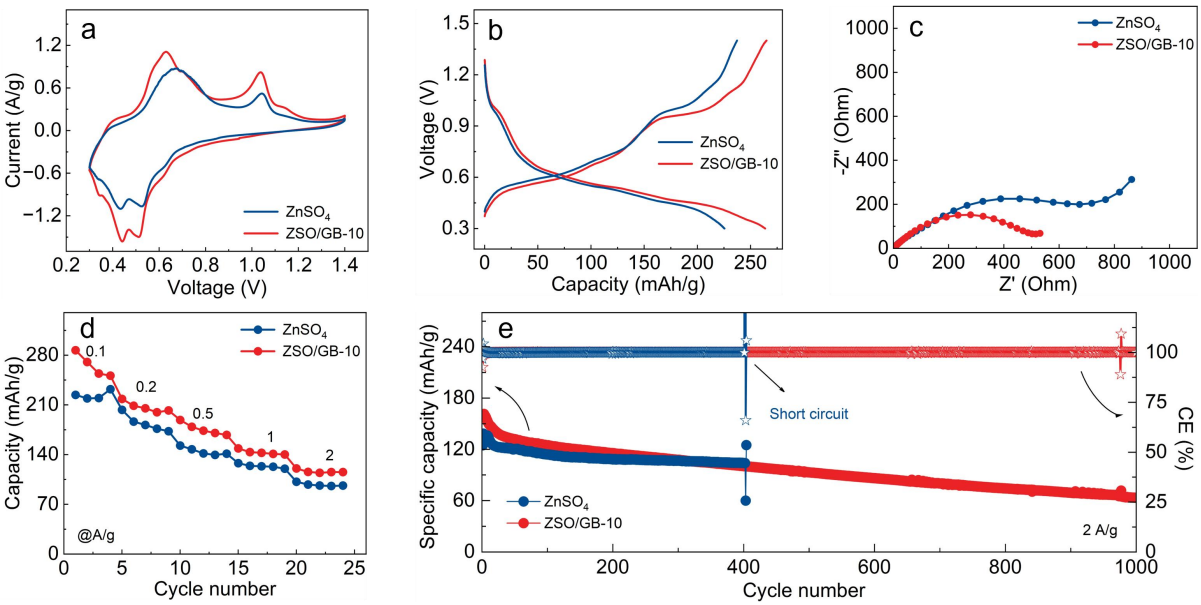

Figure S25. Electrochemical performance of VO_2//Zn ZIBs assembled with the $ZnSO_4$ and ZSO/GB-10 electrolytes: (a) CV curves at 0.5 mV/s; (b) GCD profiles at 0.1 A/g; (c) EIS spectra; (d) Rate performance; (e) Cycling tests at 2 A/g.

Table S1. Cycling performance of zinc anodes in various electrolytes reported in literature

Zinc-salt electrolyte with various additives	Testing conditions		Lifespan (h)	Cumulative capacity (Ah/cm^2)	*Ref.*
	Current (mA/cm^2)	Capacity (mAh/cm^2)			
2 M $ZnSO_4$+10 mM GB	1	0.2	2100	1.05	This work
	5	1	1100	2.63	
	10	2	730	3.65	
1 M $ZnSO_4$+100 mM NA	1	1	2500	1.25	[S1]
	8	8	700	2.80	
1 M $ZnSO_4$+ 10% TG	1	0.5	1100	0.55	[S2]
	2	0.67	1000	1.00	
2 M $ZnSO_4$+ 40 μL/mL Diethylenetriamine	0.5	0.5	2000	0.50	[S3]
	1	1	1100	0.55	
2 M $ZnSO_4$+10 mM Dodecyltrimethyl ammonium chloride	1	1	2000	1.00	[S4]
	5	5	500	1.25	
	10	5	500	2.50	
2 M $ZnSO_4$/Carboxymethyl cellulose/tannic acid hydrogel electrolyte	0.5	0.25	2109	0.53	[S5]
	1	1	720	0.36	
2 M $ZnSO_4$+0.2 M Disodium succinate	1	1	2300	1.15	[S6]
	5	5	500	1.25	
2 M $ZnSO_4$ + 0.05 M L-carnosine	1	1	5400	2.70	[S7]
	5	5	1100	2.75	
$Zn(ClO_4)_2 \cdot 6H_2O$+β-CD+ H_2O (7: 4.5: 3)	0.5	0.5	900	0.23	[S8]
	1	1	700	0.35	
2 M $ZnSO_4$ +0.1 M 3-(1-pyridinio)-1-propanesulfonate	3	3	500	0.75	[S9]
2 M $ZnSO_4$ +0.1 M Xylose	1	0.5	2000	1.00	[S10]
	5	2.5	300	0.75	
1 M $ZnSO_4$+ Epicatechin	1	1	1400	0.70	[S11]
	2	2	370	0.37	
1 M $ZnSO_4$+20 mg Polyoxometalates	1	1	2000	1.00	[S12]
	5	1	580	1.45	
2 M $ZnSO_4$ +50 mM 1-butyl-3-methylimidazolium hexafluorophosphate	1	1	800	0.40	[S13]
	4	0.5	1000	2.00	

References

[S1] H. Liang. J. Wu, J. Li, J. Wang, Z. Yang, Y. Wu, *Small* **2024**, 20, 2402595.

[S2] Z. Liu, R. Wang, Q. Ma, J. Wan, S. Zhang, L. Zhang, H. Li, Q. Luo, J. Wu, T. Zhou, J. Mao, L. Zhang, C. Zhang, Z. Guo, *Adv. Funct. Mater.* **2024**, 34, 2214538.

[S3] X. Gong, H. Yang, J. Wang, G. Wang, J Tian, *ACS Appl. Mater. Interfaces* **2023**, 15, 4152.

[S4] X. Zhang, L. Chen, R. Orenstein, X. Lu, C. Wang, M. Yanilmaz, M. Peng, Y. Dong, Y. Liu, X. Zhang, *Energy Storage Mater.* **2024**, 70, 103500.

[S5] X. Li, Y. Li, R. Wang, D. Wang, F. Ran, *Chem. Eng. J.* **2024**, 496, 153865.

[S6] Y. Ding, L. Yin, T. Du, Y. Wang, Z. He, J. Yuwono, G. Li, J. Liu, S. Zhang, T. Yang, Z. Guo, *Adv. Funct. Mater.* **2024**, 34, 2314388.

[S7] Z. Chen, Y. Xu, R. Jiang, H. Zhu, Q. Zhang, L. Ma, C. Zhang, L. Zhou, W. Wei, *Adv. Funct. Mater.* **2025**, e12356.

[S8] M. Cheng, D. Li, J. Cao, T. Sun, Q. Sun, *Angew. Chem. Int. Ed.* **2024**, 63, e202410210.

[S9] C. Jiang, M. Li, J. Fan, X. Zhu, C. Song, Z. Li, G. Xu, F. Du, H. Wang, M. Wu, C. Pei, H. Fu, G. Wang, *Nano Energy* **2025**, 111178.

[S10] X. Li, J. Xiang, L. Qiu, X. Chen, Y. Zhao, Y. Wang, Q. Yue, T. Gao, W. Liu, D. Xiao, Z. Jin, P. Li, *J. Energy Chem.* **2025**, 100, 770.

[S11] M. Yang, J. Zhu, S. Bi, R. Wang, H. Wang, F. Yue, Z. Niu, *Angew. Chem. Int. Ed.* **2024**, 63, e202400337.

[S12] Y. Chen, Z. Zhang, P. Cai, Z. Guo, Z. Lu, C. Sun, X. Li, J. Chen, Z. Wen, S. Zheng, *Angew. Chem. Int. Edit.* **2025**, 137, e202420284.

[S13] C. Shen, Y. Zhang, X. Li, P. Guo, X. Zeng, K. Ni, R. Cao, Z. Wang, Z. Wang, L. Qin, *J. Mater. Chem. A* **2025**, 13, 2174.